THE JOURNAL OF PHYSICAL CHEMISTRY LETTERS
A JOURNAL OF THE AMERICAN CHEMICAL SOCIETY

pubs.acs.org/JPCL Letter

Imaging Charged Exciton Localization in van der Waals $WSe_2/MoSe_2$ Heterobilayers

Matthew Gabel, Patrick Z. El-Khoury, and Yi Gu*

Cite This: *J. Phys. Chem. Lett.* 2021, 12, 10589−10594 Read Online

ACCESS | Metrics & More | Article Recommendations | Supporting Information

ABSTRACT: Exciton localization in transition-metal dichalcogenide monolayers is behind a variety of interesting phenomena and applications, including broad-spectrum solar cells and single-photon emissions. Strain fields at the periphery of topographically distinct features such as nanoscopic bubbles were recently associated with localized charge-neutral excitons. Here, we use tip-enhanced photoluminescence (PL) to visualize excitons in $WSe_2/MoSe_2$ heterobilayers (HBL). We find strong optical emission from charged excitons, particularly positively charged trions, in HBL supported by interlayer charge transfer. Our results reveal strong trion confinement, with a localization length scale comparable to the trion size, at the apex region inside individual nanoscopic bubbles. Nano-PL mapping also shows sub-10-nm spatial variations in the localized trion emission spectra, which stem from atomic-scale potential energy fluctuations. These findings demonstrate the possibility of confining charged exciton complexes that are electrically tunable, opening up further opportunities to probe many-body exciton physics and to explore additional possible sites for strong exciton localization that can lead to quantum emission.

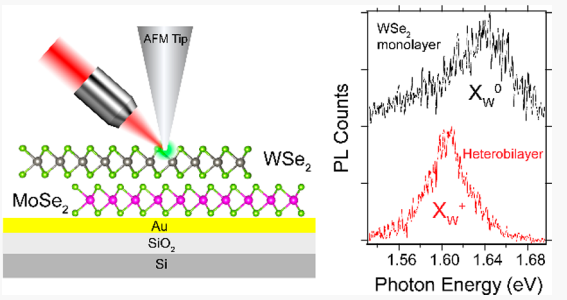

Two-dimensional (2D) transition-metal dichalcogenides (TMDC) provide a unique platform to advance the existing understanding of the interaction between light and low-dimensional quantum materials. The latter is a common theme in modern lasers and photovoltaic and (micro)-electronic devices that harness the unique properties of TMDCs. The large excitonic binding energy in TMDC monolayers due to reduced dielectric screening allows access to excitons and various excitonic complexes (such as trions and biexcitons), which provides opportunities for understanding and exploiting rich exciton physics under ambient conditions.[1−5] In addition to these intralayer excitons, interlayer excitons have been documented in type-II band structures in vertical TMDC heterostructures.[6−8] In this context, controlling exciton dynamics has been a focus of recent efforts,[9,10] with the aim of enabling novel exciton-based optoelectronic devices. Among the various approaches that are being explored to date, strain engineering[11−13] is a promising route toward efficiently controlling exciton emission energies as well as exciton localization and funneling.

As the strain-induced exciton phenomena often occur on the nanoscale, for example, inside nanosized bubbles in monolayers,[14,15] the capability to directly link exciton emission characteristics with local topographic properties is critical and requires spatial resolution much beyond that of conventional/diffraction-limited/far-field optical techniques. Such spatial resolution can be achieved by tip-enhanced optical spectroscopy, wherein optical field localization at the apex of a plasmonic probe (e.g., of an atomic force microscope or AFM) may be used to enhance both incident and scattered optical radiation.[16−19] Using this scheme, it was recently demonstrated that atomic-scale wrinkles at the periphery of nanobubbles serve as exciton localization sites.[20] Similarly, the manipulation of local strain fields and heterostructure architectures was used to control exciton localization and emission.[21,22]

In this work, we use hyperspectral nanophotoluminescence (nano-PL) to image excitonic emission from WSe_2 (top layer)/$MoSe_2$ (bottom layer) heterobilayer structures. We observe strong localization of positively charged trions of the WSe_2 layer inside individual heterostructure nanobubbles. As previous studies have mostly focused on simple (i.e., charge-neutral) exciton localizations, our findings validate the possibility of strongly confined charged exciton complexes, thus further expanding the promise of room-temperature quantum emission that can be tuned using external electrical fields.

The schematics of the sample structure with (a) the type-II band alignment[23] and (b) the nano-PL approach are shown in Figure 1. $WSe_2/MoSe_2$ vertical heterobilayers grown by

Received: September 20, 2021
Accepted: October 20, 2021

https://doi.org/10.1021/acs.jpclett.1c03093
J. Phys. Chem. Lett. 2021, 12, 10589−10594

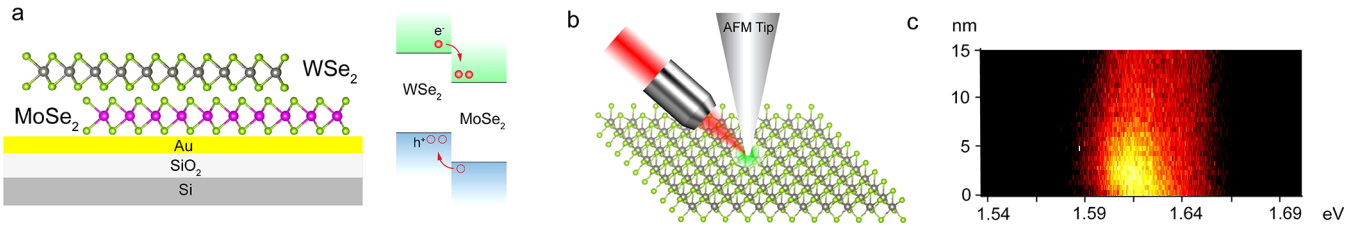

Figure 1. Schematics of (a) heterobilayer structure with the type-II band alignment and (b) tip-enhanced PL spectroscopy. (c) PL spectra as a function of the tip−surface distance.

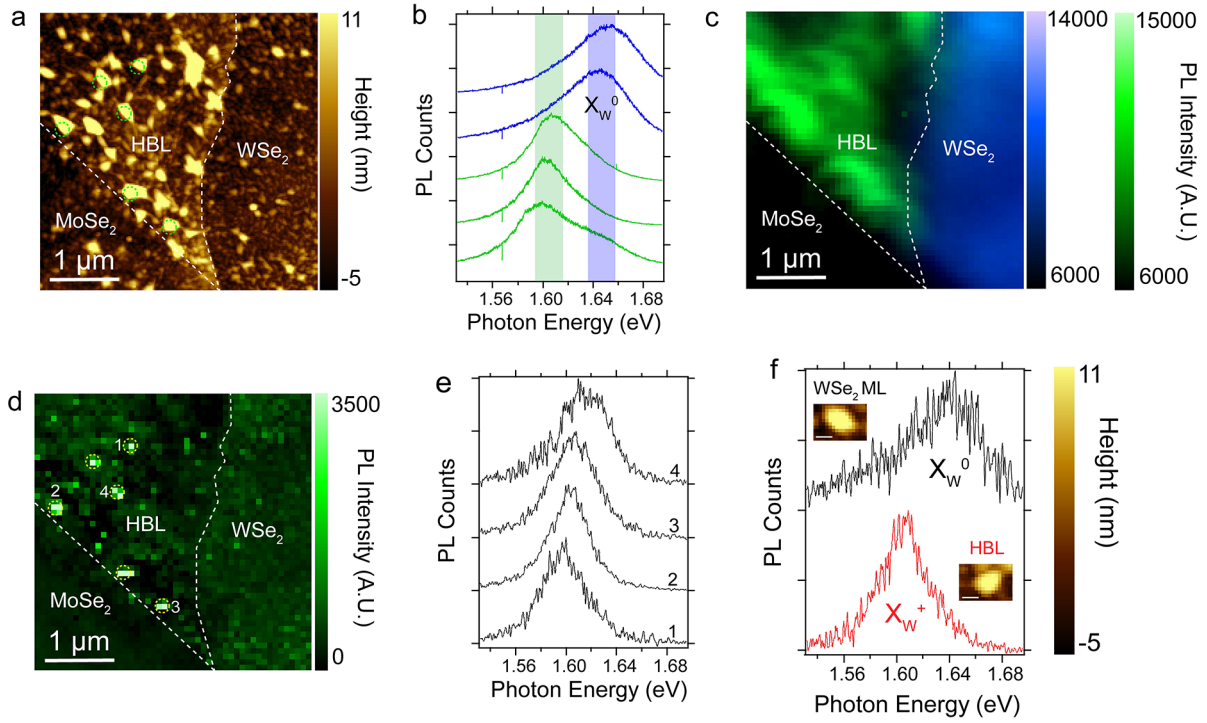

Figure 2. (a) AFM image. (b) μ-PL spectra collected from the WSe_2 ML (blue curves) and the HBL (green curves). (c) μ-PL map of the X_W^0 and 1.60 eV peak areas marked by the blue and green bands in (b). (d) nano-PL map of the 1.60 eV peak area marked by the green band in (b). (e) Nano-PL spectra collected from single pixels as indicated in (d). (f) Nano-PL spectra collected from individual bubbles (with AFM images shown in the inset) in WSe_2 ML and HBL regions. Circles in (a) and (d) highlight the same areas corresponding to the hot spots of the 1.60 eV emission. Scale bars in the insets to (f): 100 nm.

chemical vapor deposition were purchased from a commercial source (*2D Semiconductors*). The as-received samples were annealed in Ar at 100 °C for 1 h to improve interlayer coupling. Nano-PL imaging was carried out using a previously described AFM optical setup.[24,25] Details of the measurements reported herein can be found in Methods. Figure 1c shows PL spectra from the HBL region (see also below) as a function of the tip−sample distance, with the force (represented by AFM cantilever deflection)−distance curve shown in Figure S1 in the Supporting Information. The tip-enhanced effect is evident when the tip−sample distance is less than ∼5 nm, which is consistent with the inferred spatial resolution that was recently reported using the same setup.[25]

Both WSe_2 and $MoSe_2$ layers show characteristic charge-neutral band-edge exciton emission in their far-field micro-PL (μ-PL) spectra (Figure S2 in the Supporting Information), which is consistent with the monolayer (ML) configuration. That said, we find that the emission from WSe_2 MLs is usually stronger than that from $MoSe_2$ MLs, as observed in CVD-grown layers.[7] Figure 2a shows an AFM image of WSe_2 and $MoSe_2$ ML and $WSe_2/MoSe_2$ heterobilayer (HBL) regions of the sample. Distinct topographic features, in particular, nanobubbles, are observable in areas all across the substrate. These bubbles are likely to have formed during layer transfer[15] and may also be affected by the surface roughness of the underlying Au substrate. The bubbles in the WSe_2 and $MoSe_2$ MLs are typically ∼80−210 nm wide and ∼5−20 nm tall, and those in the HBL region have a variety of sizes ranging from ∼100 to 300 nm in width and ∼5 to 25 nm in height. The density of the bubbles is greater in the HBL region than in the MLs. This can be attributed to the formation of additional bubbles during layer transfer as well as the superposition of bubbles from both ML regions.

Figure 2b compares the μ-PL spectra from the HBL and WSe_2 ML regions. Figure S3 in the Supporting Information shows the HBL and $MoSe_2$ ML μ-PL spectra. A distinctive emission peak at ∼1.60 eV can be observed in the HBL, in contrast to the neutral exciton emission (X_W^0) at ∼1.65 eV from the adjacent WSe_2 ML region. We did not observe the interlayer excitonic emissions as reported in previous studies.[6−8] This might be due to the residual contamination at the interface. Another possible mechanism is that the 1.60

https://doi.org/10.1021/acs.jpclett.1c03093
J. Phys. Chem. Lett. 2021, 12, 10589−10594

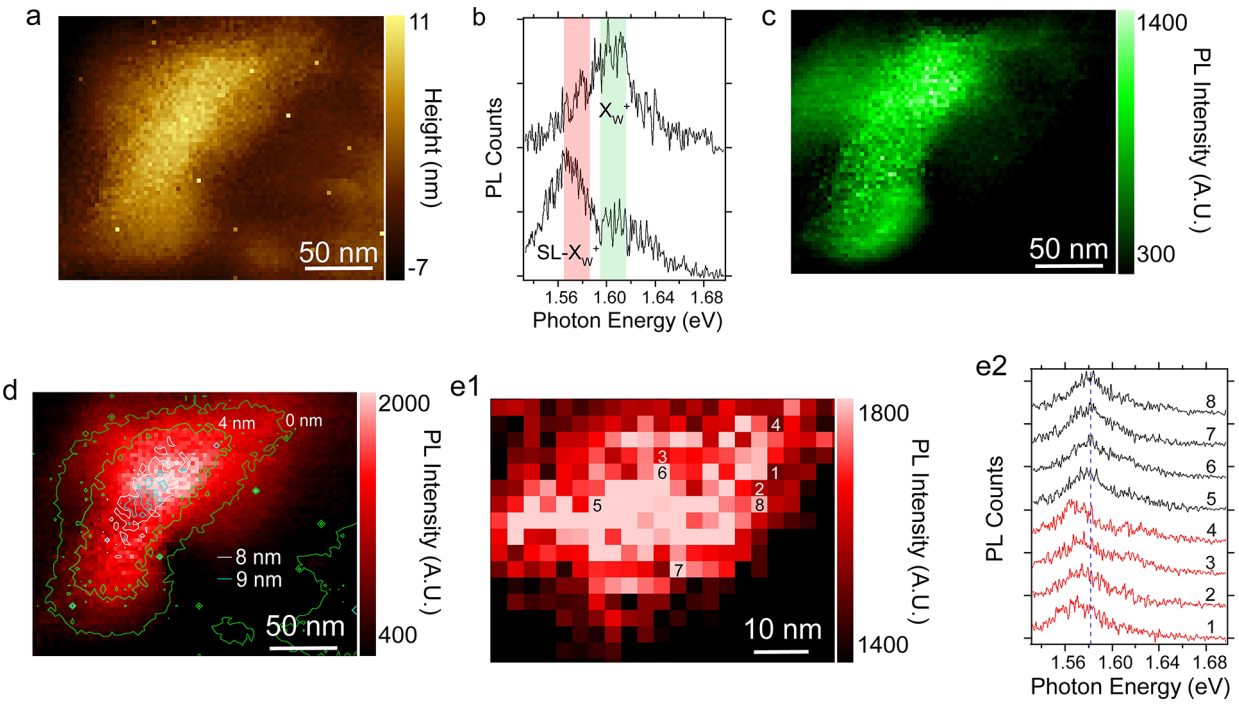

Figure 3. (a) AFM image of an HBL bubble. (b) Nano-PL spectra collected from different areas inside the bubble. Nano-PL map of the (c) X_W^+ emission and (d) SL-X_W^+ emission peak areas marked by the green and red bands in (b), respectively, with the contour topography plot of the bubble superimposed in (d). (e1) Region with the strongest SL-X_W^+ emission. (e2) Nano-PL spectra collected from single pixels as indicated in (e1).

eV emission (see also below) is enhanced in the HBL region at the expense of the interlayer exciton (as well as the charge-neutral exciton) emission, given the relatively slow radiative recombination rate of interlayer excitons.[6] The difference in optical emission from the HBL and WSe_2 ML regions is visualized in Figure 2c, with the blue (green) color scale representing the peak area under the blue (green) band in Figure 2b. While the emissions from the HBL region are dominated by the 1.60 eV peak, the spatial inhomogeneity of its intensity can be clearly observed.

Greater details of the emission characteristics are revealed in nano-PL maps (Figure 2d) of the same sample, with the green color scale corresponding to the area of the 1.60 eV peak marked by the green band in Figure 2b. The intensity of the 1.60 eV emission in the HBL region shows significant spatial variations, with the "hot spots" (i.e., regions with enhanced emission intensities) correlated to topographical features, particularly bubbles, as indicated by circles in Figure 2a,d. The comparison between the nano-PL spectra from inside and outside a bubble is shown in Figure S4 in the Supporting Information. There are also some emission energy variations (~1.60−1.62 eV) resolved by nano-PL mapping, as shown from the spectra (Figure 2e) encoded in individual pixels in Figure 2d. We note that, as the layers are suspended inside the bubble, the tip−surface interaction could have a potential impact on the PL spectra. In a previous study,[21] an AFM tip was deliberately pushed into an existing wrinkle of the WSe_2 monolayer; the resulting PL energy shift is ~2 meV with the tip pushed ~10 nm into the wrinkle. In our case, we expect a weaker tip−surface force and thus a minimal impact on the PL energy shift. Additional PL hot spots and associated spectra are presented in Figure S5 in the Supporting Information. On the basis of our observations, nearly all of the PL hot spots are associated with bubbles, and not all of the bubbles exhibit enhanced PL (most of them do, however). While more studies are needed to understand why some of the bubbles are optically dark, one possibility is that these bubbles might be structurally different (e.g., due to a high degree of mechanical deformation) so that there are significant changes in band structures and defect characteristics/generations, suppressing PL emission. By comparing Figure 2c,d, nano-PL imaging identifies the presence of nanoscopic bubbles and associated enhanced emissions as the origin of the spatial inhomogeneity in the far-field μ-PL map. Similar hot spots in the X_W^0 emission were also observed in the WSe_2 ML region (Figure S6 in the Supporting Information).

To identify the origin of the 1.60 eV emission, here we consider possibilities that include biexcitons, defects, strain-shifted neutral excitons, and negative and positive trions. The energy separation between the 1.60 eV emission (~30−50 meV) and the X_W^0 emission is close to the binding energy of biexcitons in WSe_2.[5,26] However, a recent study[16] clearly showed that biexciton emission begins to emerge only at high excitation intensities on the order of 10^7 W/cm^2 in WSe_2, which is 3 orders of magnitude higher than that used for the far-field μ-PL spectra (Figure 2b). For defect-related origins, such emissions should be present in both ML WSe_2 and HBL regions, which is in contrast to our observations. To evaluate the possibility of strain-shifted neutral excitons, we chose two bubbles with similar dimensions (and thus with similar strain profiles) from WSe_2 ML and HBL regions. As shown in Figure 2f, nano-PL spectra show distinctive 1.60 eV and X_W^0 emissions from individual HBL and WSe_2 ML bubbles, respectively, with the AFM images of these two bubbles shown in the inset. This suggests that the 1.60 eV emission is unlikely to be due to the strain-shifted X_W^0 emission.[22] The negative trion emission is also unlikely given the exclusive presence of the 1.60 eV peak in HBL. We note that, in WSe_2/

https://doi.org/10.1021/acs.jpclett.1c03093
J. Phys. Chem. Lett. 2021, 12, 10589−10594

MoS_2 and $WSe_2/MoSe_2$ heterostructures, both of which have a type-II band alignment, similar peaks close to 1.60 eV were recently observed.[22] In light of the discussions above, the appearance of similar emissions in WSe_2 overlaid on different layers (MoS_2 and $MoSe_2$) points to the dominant role of band alignment. As the type-II band alignment supports the hole (electron) transfer from the $MoSe_2$ (WSe_2) to the WSe_2 ($MoSe_2$) layer, as shown in Figure 1a, we suggest that the positive trion emission (X_W^+) is the most likely origin of the 1.60 eV peak.

To gain further insight into the nanoscale characteristics of the X_W^+ emissions inside the hot spots, we conducted high-spatial-resolution scans of a bubble shown in Figure 3a, with a lateral step size of 3 nm. Interestingly, some of the PL spectra collected from single pixels across the bubble show another peak at around 1.57−1.58 eV in addition to the X_W^+ emission (see, e.g., Figure 3b). The intensity ratio between these two peaks varies inside the bubble. In particular, the nano-PL mapping shows that the X_W^+ emission intensity, measured from the peak area under the green band in Figure 3b, remains rather uniform throughout the entire bubble area (Figure 3c). Conversely, the intensity of the 1.57−1.58 eV emission peak (marked by the red band in Figure 3b) exhibits significant spatial variations inside the bubble. As shown in Figure 3d, the shape of such variations conforms very closely to the contour lines of the bubble topography. In particular, the area with the strongest emission intensity appears mostly inside the highest region (top) of the bubble. This strong correlation to the topography is characteristic of the strain-induced exciton funneling effect.[13] Similar results were obtained on a round-shaped bubble (Figure S7 in the Supporting Information), where we also observed lower (higher) PL emission energy toward the center (periphery) of the bubble.

To evaluate the possible strain-related effects, we estimate the strain inside the nanoscale bubble shown in Figure 3a. Because of the elongated shape of the bubble (∼125 nm × 210 nm), as an approximation, we consider the strain to be largely uniaxial. The maximum tensile strain, $\varepsilon_{t,max}$, at the apex of the bubble can be estimated using the following relation[21]

$$\varepsilon_{t,max} = \frac{\pi^2 \delta h}{\lambda^2(1-\sigma^2)} \quad (1)$$

with δ, h, λ, and σ being the bubble height, layer thickness, bubble width, and Poisson's ratio of WSe_2, respectively.[21] With a base width and height of ∼125 nm and ∼11.5 nm, respectively, and with a Poisson's ratio of 0.19,[23] ε_t of this bubble is ∼0.75%. This tensile strain leads to a reduction of ∼37.5 meV in the band gap (i.e., $\Delta E_g \approx -37.5$ meV), assuming a linear relation between ΔE_g and ε_t with a proportionality ratio of ∼−50 meV/%.[21] As the energy shift (∼−20 to −50 meV) of the 1.57−1.58 eV peak from the X_W^+ emission agrees well with strain-induced ΔE_g and given the close correlation between its intensity and the bubble topography, we assign the 1.57−1.58 eV peak to be the strain-localized trion emission (i.e., SL-X_W^+), the intensity of which is enhanced by the exciton funneling effect.[13] While previous far-field PL mapping has shown the charge-neutral exciton diffusion/localization under a strain field,[13] our results provide direct evidence that the strong localization of trions occurs within the small apex region (∼30 × 40 nm^2) of an individual bubble.[27] For a perspective on the degree of this trion localization, we can compare the dimensions of the spatial confinement with the trion Bohr radius. As the radius of the charge-neutral exciton in WSe_2 is ∼1 to 2 nm[28] and its binding energy is roughly 1 order of magnitude larger than that of trions, the trion Bohr radius can be estimated to be close to 10 nm. Therefore, the length scale of the trion localization is comparable to the trion size, indicating strong confinement.

Closer inspections of the SL-X_W^+ emission inside the apex regions (Figure 3e1,e2) reveal very similar spectra (black curves) across "bright" pixels that are separated from each other, suggesting the consistency of our nano-PL mapping measurements. There are, however, "dark" pixels interspersed inside the apex region. Spectra collected from these pixels (red curves in Figure 3e2) are distinct from those from the bright pixels. In particular, the emission energy is lower by ∼6−13 meV at the dark pixels compared to their bright analogues. With the 3 nm lateral step size, this points to the energy variations on the sub-10-nm scale; such variations are tentatively due to point defects or surface roughness within the small apex area. The identification of the exact structural origin of the observed variations requires further studies such as correlated electron microscopy and nano-PL mapping.

In summary, through tip-enhanced nano-PL imaging, we were able to identify photoluminescence arising from positively charged trions supported by interlayer charge transfer in a TMDC heterobilayer structure. Such emissions are greatly enhanced inside nanoscale bubbles, and our results have shown strong strain-induced confinement of these trions with a localization length scale comparable to their sizes. Furthermore, sub-10-nm spatial variations were observable among strain-localized trion emission spectra, indicating possible atomic-scale mechanisms and phenomena such as point-defect-related potential energy fluctuations. The possibility of strongly confining charged exciton complexes, the properties of which can be controlled by an external electric field, opens opportunities to study tunable many-body interactions and to create new solid-state quantum emitters.

METHODS

Measurements were performed using a previously described setup and measurement protocol.[25] For the purpose of this work, spectra were recorded following 633 nm laser irradiation using a laser fluence of 2.5 × 10^4 W/cm^2 with an integration time of 0.25 s/pixel and an NF shift (amplitude) of 20 (Figures 3, S1, and S3) and a laser fluence of 1.5 × 10^4 W/cm^2 with an integration time of 0.5 s/pixel and an NF shift of 20 (Figures 2 and S2). An oscillation amplitude of 20−40 nm was used in the AFM scans. The P-polarized 150 μW laser source was focused on the sample using a Mitutoyo 100×/NA = 0.7 air objective at 65° with respect to the sample normal, collected back through the same objective, and filtered with a series of cleanup filters. The final signal was collected using an Andor Newton EMCCD camera coupled to an Andor Shamrock 500 spectrometer with a 300 line/mm grating blazed at 550 nm. The tips that were used were purchased (silicon ATEC-NC) and coated with 100 nm of Au using physical vapor deposition. Since the spectral data for the nano-PL when the tip is in contact with the sample also includes a response from the larger-area far-field illumination, the far-field PL spectra were subtracted (within the AIST-NT software) from the near-field PL spectra at equivalent pixels, leaving a pure near-field PL signal, as noted in the text.[25] The spectra were otherwise smoothed using 10-point (across a wavelength range of ±0.25 nm) adjacent averaging.

https://doi.org/10.1021/acs.jpclett.1c03093
J. Phys. Chem. Lett. 2021, 12, 10589−10594

■ ASSOCIATED CONTENT

Supporting Information

The Supporting Information is available free of charge at https://pubs.acs.org/doi/10.1021/acs.jpclett.1c03093.

Force−distance curve obtained from the same spot where the PL spectra in Figure 1c was recorded; far-field μ-PL spectra from WSe_2 ML and $MoSe_2$ ML; μ-PL spectra collected from the HBL and $MoSe_2$ ML regions; comparison of nano-PL collected inside and outside a bubble in the HBL region; reproduced nano-PL map, AFM image, and nano-PL spectra; nano-PL map of the X_W^0 peak area marked by the blue band in Figure 2(b); and nano-PL maps of the X_W^+ and SL-X_W^+ peak areas marked by the green and red bands in Figure 3(b) (PDF)

■ AUTHOR INFORMATION

Corresponding Author

Yi Gu − *Department of Physics and Astronomy, Washington State University, Pullman, Washington 99164, United States;* orcid.org/0000-0001-7241-9888; Email: yigu@wsu.edu

Authors

Matthew Gabel − *Department of Physics and Astronomy, Washington State University, Pullman, Washington 99164, United States*

Patrick Z. El-Khoury − *Physical Sciences Division, Pacific Northwest National Laboratory, Richland, Washington 99352, United States;* orcid.org/0000-0002-6032-9006

Complete contact information is available at: https://pubs.acs.org/10.1021/acs.jpclett.1c03093

Notes

The authors declare the following competing financial interest(s): Yi Gu is an advisor for Klar Scientific and has equity interest in the company.

■ ACKNOWLEDGMENTS

M.G. and Y.G. acknowledge the support from U.S. National Science Foundation (CMMI-1930769). P.Z.E.-K. acknowledges support from the United States Department of Energy, Office of Science, Office of Basic Energy Sciences, Division of Chemical Sciences, Geosciences & Biosciences.

■ REFERENCES

(1) Chernikov, A.; Berkelbach, T. C.; Hill, H. M.; Rigosi, A.; Li, Y. L.; Aslan, O. B.; Reichman, D. R.; Hybertsen, M. S.; Heinz, T. F. Exciton Binding Energy and Nonhydrogenic Rydberg Series in Monolayer WS_2. *Phys. Rev. Lett.* **2014**, *113*, 076802.

(2) Ugeda, M. M.; et al. Giant Bandgap Renormalization and Excitonic Effects in a Monolayer Transition Metal Dichalcogenide Semiconductor. *Nat. Mater.* **2014**, *13*, 1091−1095.

(3) Mak, K. F.; He, K. L.; Lee, C.; Lee, G. H.; Hone, J.; Heinz, T. F.; Shan, J. Tightly Bound Trions in Monolayer Mos2. *Nat. Mater.* **2013**, *12*, 207−211.

(4) Berkelbach, T. C.; Hybertsen, M. S.; Reichman, D. R. Theory of Neutral and Charged Excitons in Monolayer Transition Metal Dichalcogenides. *Phys. Rev. B: Condens. Matter Mater. Phys.* **2013**, *88*, 045318.

(5) You, Y. M.; Zhang, X. X.; Berkelbach, T. C.; Hybertsen, M. S.; Reichman, D. R.; Heinz, T. F. Observation of Biexcitons in Monolayer WSe_2. *Nat. Phys.* **2015**, *11*, 477−U138.

(6) Rivera, P.; et al. Observation of Long-Lived Interlayer Excitons in Monolayer $MoSe_2$-WSe_2 Heterostructures. *Nat. Commun.* **2015**, *6*, 6242.

(7) Nayak, P. K.; et al. Probing Evolution of Twist-Angle-Dependent Interlayer Excitons in $MoSe_2$/WSe_2 Van Der Waals Heterostructures. *ACS Nano* **2017**, *11*, 4041−4050.

(8) Ji, J.; Delehey, C. M.; Houpt, D. N.; Heighway, M. K.; Lee, T.; Choi, J. H. Selective Chemical Modulation of Interlayer Excitons in Atomically Thin Heterostructures. *Nano Lett.* **2020**, *20*, 2500−2506.

(9) Unuchek, D.; Ciarrocchi, A.; Avsar, A.; Watanabe, K.; Taniguchi, T.; Kis, A. Room-Temperature Electrical Control of Exciton Flux in a Van Der Waals Heterostructure. *Nature* **2018**, *560*, 340.

(10) Ciarrocchi, A.; Unuchek, D.; Avsar, A.; Watanabe, K.; Taniguchi, T.; Kis, A. Polarization Switching and Electrical Control of Interlayer Excitons in Two-Dimensional Van Der Waals Heterostructures. *Nat. Photonics* **2019**, *13*, 131.

(11) Schmidt, R.; Niehues, I.; Schneider, R.; Druppel, M.; Deilmann, T.; Rohlfing, M.; de Vasconcellos, S. M.; Castellanos-Gomez, A.; Bratschitsch, R. Reversible Uniaxial Strain Tuning in Atomically Thin WSe_2. *2D Mater.* **2016**, *3*, 021011.

(12) Frisenda, R.; Druppel, M.; Schmidt, R.; de Vasconcellos, S. M.; de Lara, D. P.; Bratschitsch, R.; Rohlfing, M.; Castellanos-Gomez, A. Biaxial Strain Tuning of the Optical Properties of Single-Layer Transition Metal Dichalcogenides. *Npj 2d Materials and Applications* **2017**, *1*, 10.

(13) Moon, H.; Grosso, G.; Chakraborty, C.; Peng, C.; Taniguchi, T.; Watanabe, K.; Englund, D. Dynamic Exciton Funneling by Local Strain Control in a Monolayer Semiconductor. *Nano Lett.* **2020**, *20*, 6791−6797.

(14) Shepard, G. D.; Ajayi, O. A.; Li, X. Z.; Zhu, X. Y.; Hone, J.; Strauf, S. Nanobubble Induced Formation of Quantum Emitters in Monolayer Semiconductors. *2D Mater.* **2017**, *4*, 021019.

(15) Tyurnina, A. V.; Bandurin, D. A.; Khestanova, E.; Kravets, V. G.; Koperski, M.; Guinea, F.; Grigorenko, A. N.; Geim, A. K.; Grigorieva, I. V. Strained Bubbles in Van Der Waals Heterostructures as Local Emitters of Photoluminescence with Adjustable Wavelength. *ACS Photonics* **2019**, *6*, 516.

(16) Park, K. D.; Khatib, O.; Kravtsov, V.; Clark, G.; Xu, X. D.; Raschke, M. B. Hybrid Tip-Enhanced Nanospectroscopy and Nanoimaging of Monolayer WSe_2 with Local Strain Control. *Nano Lett.* **2016**, *16*, 2621−2627.

(17) Krayev, A.; Krylyuk, S.; Ilic, R.; Walker, A. R. H.; Bhattarai, A.; Joly, A. G.; Velicky, M.; Davydov, A. V.; El-Khoury, P. Z. Comparable Enhancement of Ters Signals from Wse2 on Chromium and Gold. *J. Phys. Chem. C* **2020**, *124*, 8971−8977.

(18) Smithe, K. K. H.; et al. Nanoscale Heterogeneities in Monolayer $MoSe_2$ Revealed by Correlated Scanning Probe Microscopy and Tip-Enhanced Raman Spectroscopy. *Acs Applied Nano Materials* **2018**, *1*, 572−579.

(19) May, M. A.; Jiang, T.; Du, C. F.; Park, K. D.; Xu, X. D.; Belyanin, A.; Raschke, M. B. Nanocavity Clock Spectroscopy: Resolving Competing Exciton Dynamics in WSe_2/$MoSe_2$ Heterobilayers. *Nano Lett.* **2021**, *21*, 522−528.

(20) Darlington, T. P.; et al. Imaging Strain-Localized Excitons in Nanoscale Bubbles of Monolayer WSe2 at Room Temperature. *Nat. Nanotechnol.* **2020**, *15*, 854.

(21) Koo, Y.; et al. Tip-Induced Nano-Engineering of Strain, Bandgap, and Exciton Funneling in 2d Semiconductors. *Adv. Mater.* **2021**, *33*, 32008234.

(22) Rodriguez, A.; Kalbac, M.; Frank, O. Strong Localization Effects in the Photoluminescence of Transition Metal Dichalcogenide Heterobilayers. *2D Mater.* **2021**, *8*, 025028.

(23) Kang, J.; Tongay, S.; Zhou, J.; Li, J. B.; Wu, J. Q. Band Offsets and Heterostructures of Two-Dimensional Semiconductors. *Appl. Phys. Lett.* **2013**, *102*, 012111.

(24) El-Khoury, P. Z.; Apra, E. Spatially Resolved Mapping of Three-Dimensional Molecular Orientations with Similar to 2 nm Spatial Resolution through Tip-Enhanced Raman Scattering. *J. Phys. Chem. C* **2020**, *124*, 17211−17217.

(25) Wang, C. F.; Zamkov, M.; El-Khoury, P. Z. Ambient Tip-Enhanced Photoluminescence with 5 nm Spatial Resolution. *J. Phys. Chem. C* **2021**, *125*, 12251−12255.
(26) Jones, A. M.; et al. Optical Generation of Excitonic Valley Coherence in Monolayer WSe_2. *Nat. Nanotechnol.* **2013**, *8*, 634−638.
(27) We note that charge carriers and excitons can diffuse from the point of generation towards the localization area where they recombine. If the diffusion process is significant (i.e., if the diffusion length is long), then the actual area of the localized emissions would be even smaller than what the nano-PL mapping has shown.
(28) Stier, A. V.; Wilson, N. P.; Clark, G.; Xu, X. D.; Crooker, S. A. Probing the Influence of Dielectric Environment on Excitons in Monolayer WSe_2: Insight from High Magnetic Fields. *Nano Lett.* **2016**, *16*, 7054−7060.

https://doi.org/10.1021/acs.jpclett.1c03093
J. Phys. Chem. Lett. 2021, 12, 10589−10594